Ultrasonics 91 (2019) 103–113

Contents lists available at ScienceDirect

Ultrasonics

journal homepage: www.elsevier.com/locate/ultras

An improved Richardson-Lucy iterative algorithm for C-scan image restoration and inclusion size measurement

Dan Chen[a,b], Huifang Xiao[a,*], Jinwu Xu[b]

[a] School of Mechanical Engineering, University of Science and Technology Beijing, Beijing 100083, PR China
[b] Collaborative Innovation Center of Steel Technology, University of Science and Technology Beijing, Beijing 100083, China

ARTICLE INFO

Keywords:
Inclusion size
C-scan image
Richardson-Lucy algorithm
Point spread function
Final iteration number

ABSTRACT

The accuracy of measuring inclusion size in direct C-scan image of immersion ultrasonic testing is restricted by the lateral resolution of the focused transducer, even if a high frequency is used, and the blurred edge due to scattering of sound waves at inclusions. In this work, an improved image restoration method that is based on the Richardson-Lucy (RL) iterative algorithm is proposed, which is used to restore the C-scan image and improve the accuracy of inclusion size measurement in immersion ultrasonic testing. For the improved RL iterative algorithm, the point spread function (PSF) is derived based on the multi-Gaussian beam model and Kirchhoff approximation, which considers the propagation properties of sound waves at water-steel interface and the spectral characteristics of the transducer with high frequency. In order to determine the final iteration number, the relationship between final iteration number and size of the inclusion in the image is established by restoring the simulated C-scan image and further calibrated with size correction factor. The size correction factor considers the effect of sound attenuation and electro-mechanical transformation encountered in practical testing equipment. Experimental results show that the inclusion sizes measured in restored C-scan images agree well with the optical micrograph results, which prove the effectiveness of the proposed method.

1. Introduction

Non-metallic inclusions are formed during steel production processes and inevitably left in steel due to insufficient elimination before solidification [1]. They are the sources of different negative steel properties, such as low fatigue strength, toughness and ductility [2]. Measuring inclusion size, especially for large inclusions provides important reference for steel producing process, such as de-oxidation refining and continuous casting [3], which helps to improve the quality of steel products. In addition, inclusion size is one of the most important factors that influences the crack initiation and fatigue life of structural components [4,5]. If the maximum size of inclusions can be measured directly, rather than estimated by statistics, the fatigue limits of steel will be predicted more accurately.

In order to measure inclusion size, some methods that are based on inclusion extraction, surface analysis, fractural experiments and immersion ultrasonic testing have been proposed [6–8]. Among these methods, immersion ultrasonic C-scan imaging is the most suitable methods for determining large inclusions with a large test volume under high detection efficiency. The C-scan imaging is a top view imaging mode, which uses the amplitudes of time-series signals at one position to form the image through a 2D plane scan. However, a potential problem associated is that the C-scan image is blurred heavily, which makes it difficult to measure inclusion size accurately [9,10]. Similar problem has also been found for detecting defects in seal region of flexible food packages using normal-incidence BAI-mode imaging, in which the 95-μm water-filled channel defect exhibited a much larger size of about 200 μm [11]. Song et al. have proposed a dynamic threshold method to improve the performance of flaw sizing by ultrasonic C-scan imaging [12]. The phenomenon of C-scan image blurring is not only related to the lateral resolution of transducer, but also related to the length of focal zone in material [13]. For a body defect, only it is totally covered by the focal zone the clarity of C-scan image can reaches the highest level. However, the lateral resolution and the length of focal zone of a spherically focused transducer are inversely proportional to the center frequency [14]. The increase of frequency can improves the lateral resolution, but also reduces the length of focal zone. Moreover, the high frequency sound waves exhibit significant scattering and attenuation in steel, which leads to a poor signal-to-noise ratio (SNR). In summary, the clarity of C-scan image is inherently limited to the defects with sizes similar to or less than the wavelength.

In order to improve the clarity of C-scan image, many image

* Corresponding author.
E-mail address: huifangxiao@ustb.edu.cn (H. Xiao).

https://doi.org/10.1016/j.ultras.2018.07.021
Received 17 November 2017; Received in revised form 24 July 2018; Accepted 31 July 2018
Available online 01 August 2018

restoration techniques have been proposed, which are based on the digital signal processing or image processing. Deconvolution is one of the most important algorithms, which had been widely used in astronomy [15,16], medicine [17,18] and microscopy [19–22]. The commonly used deconvolution algorithms are Regularized inverse filtering, Tikhonov regularization, Landweber, Tikhonov Miller and Richardson-Lucy [23]. The Richardson-Lucy algorithm also known as the expectation maximization method, is an iterative scheme that computes the reflectivity function of objects from original C-scan images using a specific point spread function [24]. It has advantages of good robustness against small errors in point spread function, which can make the iteration results converge to the maximum likelihood solution. The Richardson-Lucy iterative algorithm is applicable to images that obey a Poisson distribution, especially to optical or acoustical images that contain Poisson noise. For this reason, the Richardson-Lucy algorithm has been widely used in the astronomy and microscopy [25].The point spread function (PSF) represents the response of system to a point and determines the imaging quality [26]. Assuming that ultrasonic imaging system is a linear shift-invariant system, the formation process of C-scan images is described as convolution of the reflectivity function of the object and the PSF of the imaging system. By reversing the reflectivity function of the object from an original C-scan image using an accurate PSF, the clarity of C-scan image can be improved essentially.

The PSF is one of the most important factors that determining the performance of Richardson-Lucy algorithm and significant efforts have been expended on the PSF calculation. In general, the PSF of immersion ultrasonic imaging system is either measured from a reflector that is approximately represented as a point source [27], or reconstructed via inverse filtering to a micro-sphere which has a smooth surface and a smaller diameter than the spot size of the transducer [28], or theoretically computed from the imaging models [29]. However, the experimental methods only performed in the single-phase medium like water, which lack accuracy for inclusion imaging in steel. Rangarajan et al. applied the patch element model (PEM) to compute the sound field distribution of a planar transducer and the response of a point-like reflector, the PSF in single-phase medium and liquid-solid medium was evaluated in near field and far field [29]. Dalitz et al. presented an analytical expression of PSF that is based on the far field approximation, and using the calculated PSF to restore C-scan images [26]. However, the PSF calculated by the analytical methods do not consider the spectral characteristics of transducers and the propagation properties of sound waves at water-steel interface.

In this work, an improved Richardson-Lucy iterative algorithm is proposed to restore the C-scan images measured from immersion ultrasonic imaging system using spherically focused transducer, and to improve the accuracy of inclusion sizing. The PSF is derived based on the multi-Gaussian beam model and Kirchhoff approximation that considers the refraction of sound waves at water-steel interface and the broadband characteristics of the transducer with high frequency. The relationship between final iteration number and the size of inclusion in the image is established by restored the simulated C-scan image and further calibrated with the size correction factor. Using the calculated PSF and final iteration number, the experimental C-scan images are restored using the improved RL iterative algorithm and its effectiveness has also been verified.

2. Improved Richardson-Lucy algorithm

The improved Richardson-Lucy algorithm is shown in Fig. 1, which includes the following two parts. Firstly, the PSF is calculated by a mathematical model that using the multi-Gaussian beam model [30] to compute the sound field distribution in water-steel medium and using the Kirchhoff approximation [31] to derive the expression of PSF. Secondly, the relationship between final iteration number and inclusion size in the image is established by restoring the simulated C-scan images that contain different sizes of inclusions. For the multi-Gaussian beam model, the spectral characteristics of transducer and the propagation properties of sound waves in the media of liquid and solid are considered to improve the accuracy of the PSF. The relationship between final iteration number and inclusion size in the C-scan image is further calibrated by a size correction factor, which considers the effect of sound attenuation and the electro-mechanical transformation encountered in practical ultrasonic system.

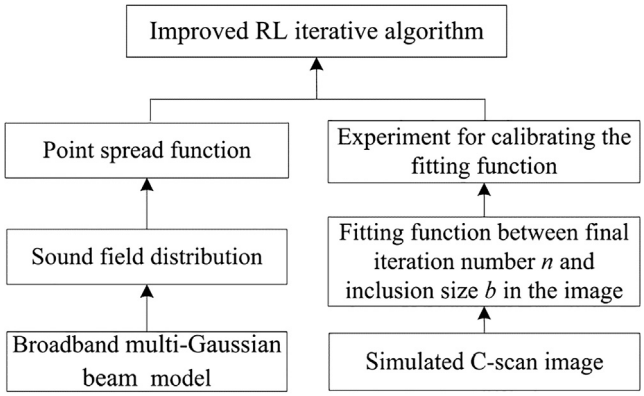

Fig. 1. The principle of the improved Richardson-Lucy iterative algorithm.

Assuming that ultrasonic C-scan imaging system is a linear shift-invariant (LSI) system, the output image I can be expressed as [32]

$$I = \zeta(f \otimes g) \tag{1}$$

where f is the object needs to be retrieved and it is represented as a reflectivity function mathematically, g is the PSF of the imaging system, $\otimes$ is the two-dimensional convolution operator, ζ represents the background noise that follows the Poisson distribution. The Eq. (1) is the commonly used ultrasonic imaging model.

The Richardson-Lucy (RL) iterative algorithm [33,34], also known as the expectation maximization method, is a Bayesian-based iterative algorithm developed for the Poisson distributed background and converged to the maximum likelihood solution. The probability density function of a pixel s in output image I, knowing $(f*g)(s)$ can be expressed as [32]

$$p\{I(s)|(f*g)(s)\} = \frac{[(f*g)(s)]^{I(s)}\exp(-(f*g)(s))}{I(s)!} \tag{2}$$

Considering all N pixels in output image I, the probability density function is a likelihood function L given by [32]

$$L = p\{I|(f*g)\} = \prod_{s=1}^{N}\left\{\frac{[(f*g)(s)]^{I(s)}\exp(-(f*g)(s))}{I(s)!}\right\} \tag{3}$$

The maximum likelihood solution occurred where all partial derivatives of L with respect to f are zeros, which leads to the RL iterative algorithm [33,34]

$$f_n = \left[\frac{I}{g*f_{n-1}}*\bar{g}\right]f_{n-1} \tag{4}$$

where $\bar{g}$ is the complex conjugate of g and n is the final iteration number. Eq. (4) shows that the restoration performance of RL algorithm mainly depends on the accuracy of PSF and the final iteration number n. In the following sections, the process of PSF calculation and the determination of final iteration number n are described in detail. The PSFs of the transducers with center frequency of 50 MHz and 100 MHz are calculated, respectively, and the relationships between final iteration number and size of inclusion in the simulated C-scan image are established.

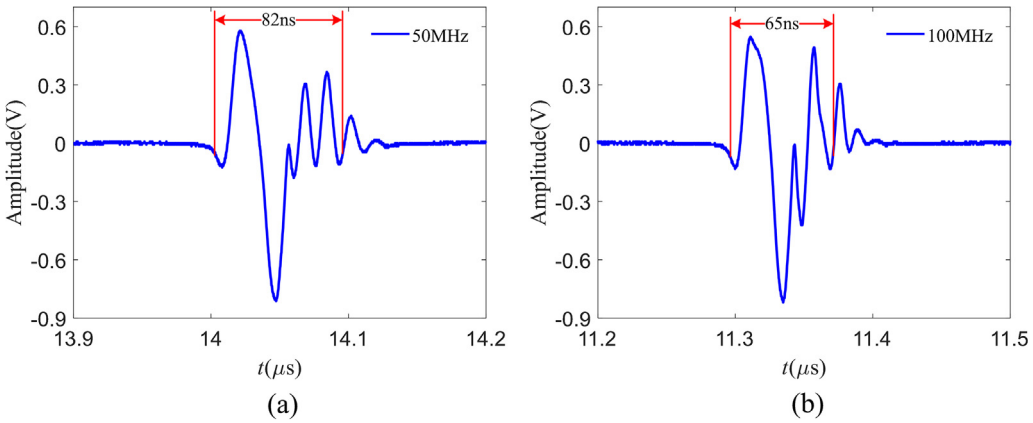

Fig. 2. Signals of interface wave reflected by the top surface of a bearing steel ball using different spherically focused transducers (a) 50 MHz nominal center frequency and 10 mm focal length (b) 100 MHz nominal center frequency and 8 mm focal length.

2.1. Calculation of PSF

The PSF is derived based on the Multi-Gaussian beam model and Kirchhoff approximation, which considers the refraction of sound waves at water-steel interface, as well as the spectral characteristics of broadband transducer. The relationship between PSF g and sound field distribution H is established by using the Kirchhoff approximation and expressed as [26]

$$g(x, y) = \frac{i\omega\rho v_0}{4\pi^2} H(z_0, x, y) \frac{\partial}{\partial z} H(z, x, y)|_{z=z_0} \tag{5}$$

where v_0 is the velocity amplitude of transducer oscillating with frequency $f = \omega/2\pi$, ρ is the density of medium. Eq. (5) shows that g is directly related to the sound field distribution H at the focal plane ($z = z_0$). It should be noted that the C-scan image is the maximum-intensity projection of the volumetric data. Assuming that the sound field distribution H along the z-axis is uniform within the focal area, using the PSF at focal plane is reasonable. For broadband transducer, ω is the center frequency and the sound field distribution H is a linear superposition of the sound field distribution of different frequency components.

The Multi-Gaussian beam (MGB) model, which uses Gaussian beams as their fundamental basis set and combining with a proper set of weighting factors is used to calculate the sound field distribution H of a spherically focused transducer in two media of water and steel. In this work, the spectral coefficients of transducers with broadband are considered in the MGB model, which eliminates the effect of spectral characteristics on the sound field distribution H.

According to the MGB model, the sound field distribution H_j of a single frequency component ω_j can be calculated by the equation [35]

$$H_j(x_2, y_2, z_2) = \sum_{r=1}^{15} T_{12}^{\gamma_2:p} A_r \frac{1}{1 + \frac{iB_r}{D_r}\left(z_1 + \frac{z_2 c_2^{\gamma_2}}{c_1^p}\right)} \exp\left[ik_1 z_1 + ik_2 z_2 - \frac{\frac{B_r(x_2^2 + y_2^2)}{a^2}}{1 + \frac{iB_r}{D_r}\left(z_1 + \frac{z_2 c_2^{\gamma_2}}{c_1^p}\right)} \right] \tag{6}$$

where a is the radius of piezoelectric elements, $v_2^{\gamma_2}$ is the particle velocity in medium 2, $T_{12}^{\gamma_2:p}$ is the transmission coefficient expressed as $T_{12}^{\gamma_2:p} = 2\rho_1 c_1^p/(\rho_1 c_1^p + \rho_2 c_2^{p_2})$, A_r and B_r are the Gaussian coefficients that given by literature [36], $D_r = k_1 a^2/2$ is the Rayleigh distance that refers to the distance from focus position to where the beam cross-section increases to two times the focal spot diameter [37]. k_1, c_1^p and k_2, $c_2^{\gamma_2}$ are the wavenumber and velocity of the sound waves in medium 1 and medium 2, respectively ($\gamma = p$, s), and their relationship with circular frequency ω is $k = \omega/c$.

From a discrete viewpoint, the broadband transducer has different continuously components as ω_j, $j = 1, 2, \ldots$. According to the sound field superposition principle, the sound field distribution H of a broadband transducer can be calculated by summing up the sound field distribution H_j at different frequency components ω_j

$$H(x_2, y_2, z_2) = \sum_j c_j \sum_{r=1}^{15} T_{12}^{\gamma_2:p} A_r \frac{1}{1 + \frac{iB_r}{D_r}\left(z_1 + \frac{z_2 c_2^{\gamma_2}}{c_1^p}\right)} \exp\left[ik_1 z_1 + ik_2 z_2 - \frac{\frac{B_r(x_2^2 + y_2^2)}{a^2}}{1 + \frac{iB_r}{D_r}\left(z_1 + \frac{z_2 c_2^{\gamma_2}}{c_1^p}\right)} \right] \tag{7}$$

where c_j are the spectral coefficients that describe the spectrum characteristics of the sound waves radiated from transducer and transmitted through the water medium. It is the normalized amplitude-frequency characteristics and calculated by the equation

$$c_j(\omega) = \frac{A_j(\omega)}{\sum_j A_j(\omega)} \tag{8}$$

where $A_j(\omega)$ is the amplitude of the jth frequency component that is measured from experiment. The frequency increment is determined by the sampling frequency. To calculate the spectral coefficients c_j of the broadband transducer, the interface wave reflected from a ball target is collected and the Fourier transformation is used to obtain the amplitude-frequency characteristics. The specific measurement procedures refer to the standard ASTM E1065. Substituting Eq. (7) into Eq. (5), the PSF is expressed explicitly as

$$g = \frac{i\omega\rho v_0}{4\pi^2} H^2 \left\{ \left[ik_2 + \frac{B_r(x_2^2 + y_2^2)D}{R^2 C^2} \right] - \frac{D}{C} \right\} \tag{9}$$

where

$$C = 1 + \frac{iB_r}{D_r}\left(z_1 + \frac{z_2 c_2^{\gamma_2}}{c_1^p}\right), \quad D = \frac{iB_r}{D_r}\frac{c_2^{\gamma_2}}{c_1^p}$$

Fig. 2 shows the interface wave of two spherically focused transducers with nominal center frequencies of 50 MHz and 100 MHz, respectively. The standard reflector is a bearing steel ball, which has a smooth surface and a diameter of 12 mm. The distance between transducer and the top surface of the reflector is adjusted to maximize the amplitude of interface wave. According to the ASTM E1065, the durations of the interface wave measured by −20 dB threshold are 82 ns and 65 ns. The focal lengths of the two transducers are 10 mm and

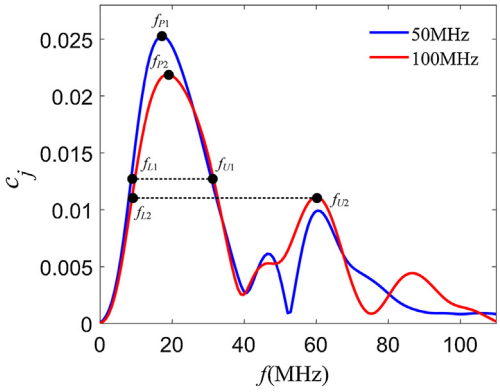

Fig. 3. The spectral coefficients of the two transducers.

8 mm in water, respectively. When the focal depths of both transducers are 0.8 mm in steel, the water paths are 6.8 mm and 4.8 mm, and the interface wave appears at 14 μs and 11.3 μs, respectively, with the longitudinal velocity in water of 1480 m/s.

The corresponding spectral coefficients c_j are shown in Fig. 3. It can be seen that both of the two transducers have a wide spectrum, the peak frequency are $f_{P1} = 17$ MHz and $f_{P2} = 20$ MHz, respectively. The lower frequency f_L and upper frequency f_U are measured by the -6dB threshold and the actual center frequency f_{C1}, f_{C2} of the two transducers calculated by $f_C = (f_U + f_L)/2$ are only 29.5 MHz and 34.5 MHz, respectively, which are far less than their nominal center frequency (50 MHz and 100 MHz). The decrease of f_{C1}, f_{C2} are mainly contribute to the severely attenuation of high frequency components in water [38].

Fig. 4 shows the on-axis pressure profile of the two transducers with broadband and mono-frequency. The horizontal axis is the vertical distance that starts from the top surface of the transducer and the vertical axis is the normalized sound pressure with respect to the maximum value of the on-axis pressure. For the two transducers the water paths are $z = 6.8$ mm and $z = 4.8$ mm, respectively. The on-axis pressure increases sharply at water-steel interface (as marked in Fig. 4). When the sound waves transmit into steel, the acoustic impedance changes from 1.5×10^6 kg/m^2 s to 45×10^6 kg/m^2 s, which leads to the on-axis pressure rising abruptly. The steep rising of the on-axis pressure profile at water-steel interface is also described in literature [39].

The maximum pressure appears at $z = 7.6$ mm and $z = 5.6$ mm, respectively, which means the refocused depths d_t inside the specimen are both 0.8 mm. The positions of the maximum pressure agree well with the theoretical refocused depths calculated by $d_t = (F - z_1)c_1/c_2^p$. The on-axis pressure profiles of the two transducers with mono-frequency and broadband are almost same near the focus, but for the mono-frequency, several nulls exist on both sides of the focus.

Fig. 5 shows the cross-axis pressure profiles of the two transducers with broadband and mono-frequency at focal plane of $z = 7.6$ mm and $z = 5.6$ mm, respectively. The horizontal axis represents the horizontal distance that is perpendicular to the axis of the transducer and it is a dimensionless distance with respect to the radius of piezoelectric elements a. It can be seen that the cross-axis pressure profiles of the two transducers with broadband and mono-frequency have a large mismatch on both sides of the focus ($x/a = 0$). For the mono-frequency, several nulls exist in the cross-axis pressure profile, but for the broadband, the cross-axis pressure profile changes smoothly. According to the additive principle of sound waves, these nulls in cross-axis pressure profile of a given mono-frequency will be filled up by the nonzero values of other frequency components, and the superposition effect leads to the nulls no longer being observed. Therefore, if the spectrum characteristics are ignored, the calculation of sound field distribution will lose some accuracy.

According to the cross-axis pressure profile, the radial profiles of PSFs for the two different transducers with broadband and mono-frequency are shown in Fig. 6. It can be seen that the radial profiles of PSFs with mono-frequency are not smooth, and two nulls exist at $x/a = \pm 0.2$ and $x/a = \pm 0.075$, respectively. But for the radial profiles of PSFs with broadband, no nulls exist and it can be represented as a Gaussian function with appropriate variance, as is described in literatures [40,41].

2.2. Determination of the final iteration number

In order to restore C-scan images using the improved RL algorithm, an appropriate final iteration number n should be chosen. The final iteration number n needs to be large enough to reach the desired solution for convergence. The convergence criterion is defined as [26]

$$\frac{\sum_x \sum_y |f_n(x, y) - f_{n-1}(x, y)|}{\sum_x \sum_y f_{n-1}(x, y)} \leqslant \Delta \tag{10}$$

where Δ is the relative error of two adjacent images, which depends on the specific images. However, the final iteration number n should not be too large to make the noise dominate. In this study the final iteration number n is chosen to guarantee the restored image as closer as to the projection of the defect. The relationship between final iteration number n and inclusion size b in simulated C-scan image is established through the following steps shown in Fig. 7.

Assuming that all inclusions have a circular projection and the C-scan images of inclusions with different size are simulated by the

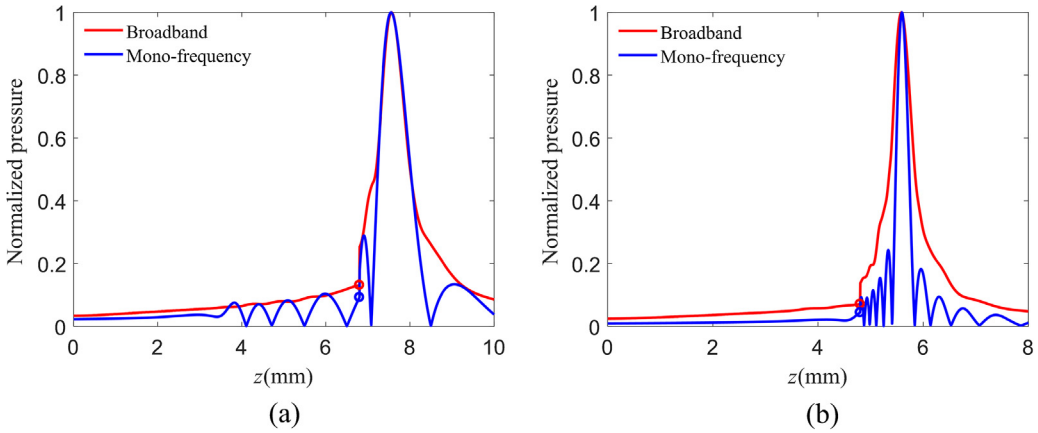

Fig. 4. The on-axis pressure profiles of two different transducers with broadband and mono-frequency (a) 50 MHz nominal center frequency and 10 mm focal length (b) 100 MHz nominal center frequency and 8 mm focal length.

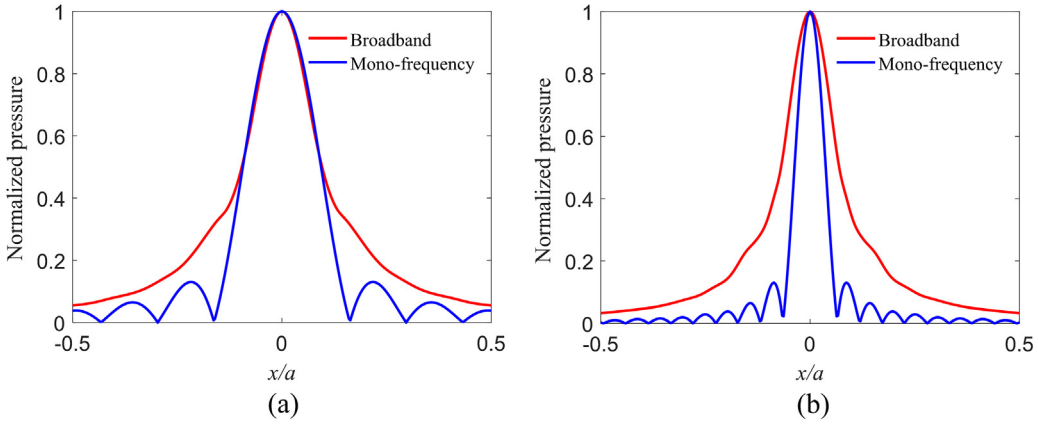

Fig. 5. The cross-axis pressure profiles of two different transducers with broadband and mono-frequency (a) 50 MHz nominal center frequency and 10 mm focal length (b) 100 MHz nominal center frequency and 8 mm focal length.

ultrasonic imaging model and the Poisson noise is added. The improved RL iterative algorithm is used to restore the simulated C-scan images, and the final iteration number n that makes inclusion size measured in restored image is equal to its true size is defined as the final iteration number. Using this method, the relationship between final iteration number n and the inclusion size b in simulated C-scan image is established.

For the above mentioned two transducers with center frequency of 50 MHz and 100 MHz, the simulated and further restored C-scan images of an inclusion with true size of 50 μm are shown in Fig. 8. Each column from left side to right side represents the PSFs of two transducers, the simulated C-scan images and the restored C-scan images. The final iteration number of the two restored C-scan images is $n = 64$ and $n = 16$, respectively. In the middle column it can be seen that the inclusion sizes b in the simulated C-scan images are much larger than their true size (50 μm). After restoration the inclusion sizes measured in restored C-scan images using 6 dB-drop threshold are 49 μm and 48 μm, respectively, which are close to their true sizes.

Fig. 9 shows the convergence of the inclusion size measured in restored C-scan images as a function of iteration numbers for different size of inclusions. The vertical axis is the inclusion size that is measured in the restored image. The true sizes of the inclusions range from 40 μm to 195 μm, which almost cover the scope of large inclusions in steel. The left figure is for the transducer of 50 MHz and the right figure is for the transducer of 100 MHz. It can be seen from Fig. 9(a) and (b), as the iteration numbers increases, the inclusion sizes measured in restored C-scan image are gradually approaching their true sizes even if the Poisson noise exists. In addition, as the iteration numbers increases, the differences between different sizes of inclusions in restored C-scan images increase, which illustrate the improvement of image clarity. As mentioned before, the RL algorithm has the problem of noise amplification with the increase of iteration number, especially for the structural noise that is aroused by the grain scattering in actual C-scan images. In order to avoid noise amplification and its effect on the measurement reliability, the final iteration number n is determined as the minimum iteration number that guarantees the inclusion size measured in restored C-scan image has the smallest error with respect to the true size, instead of the iteration number that converge. For inclusions with different sizes, the final iteration numbers n are marked in the Fig. 9(a) and (b). It should be noted that the imaging system should have sufficient measurement sensitivity and signal-to-noise ratio to make the image of inclusion clearly distinguished from the background noise and guarantee the applicable of the proposed method.

Fig. 10 shows the relationship between final iteration number n and dimensionless inclusion size b/λ_2 using transducers of center frequency of 50 MHz and 100 MHz, where λ_2 is the wavelength that is corresponding to the center frequency. The dimensionless inclusion sizes b/λ_2 measured in the original blurred images obtained by simulation range from 1.773 to 1.998 for the transducer of 50 MHz and range from 1.819 to 3.119 for the transducer of 100 MHz. According to the simulated results in Fig. 10, the relationship between final iteration number n and the dimensionless inclusion size b/λ_2 is approximately fitted to a rational function. For the transducers of 50 MHz and 100 MHz, the fitting functions are

$$n_{50}(b/\lambda_2) = \left\lceil \frac{0.824}{b/\lambda_2 - 1.755} \right\rceil \tag{11}$$

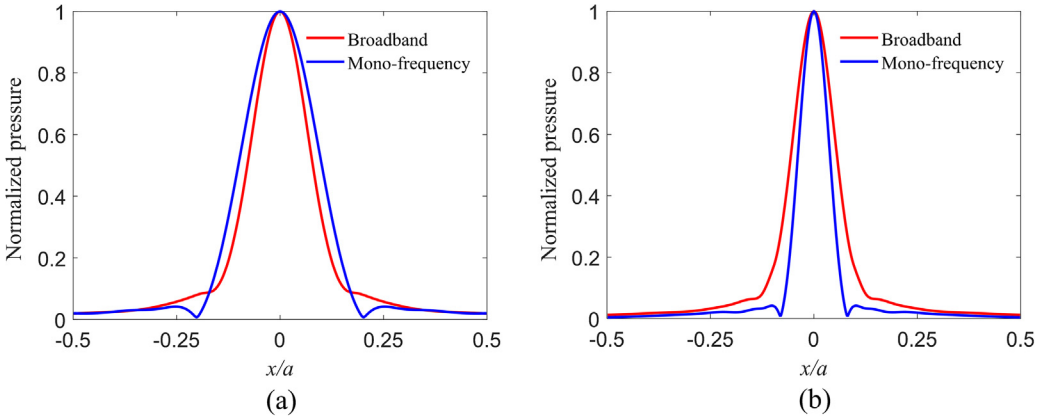

Fig. 6. The radial profiles of the PSF for different transducers with broadband and mono-frequency (a) 50 MHz nominal center frequency and 10 mm focal length (b) 100 MHz nominal center frequency and 8 mm focal length.

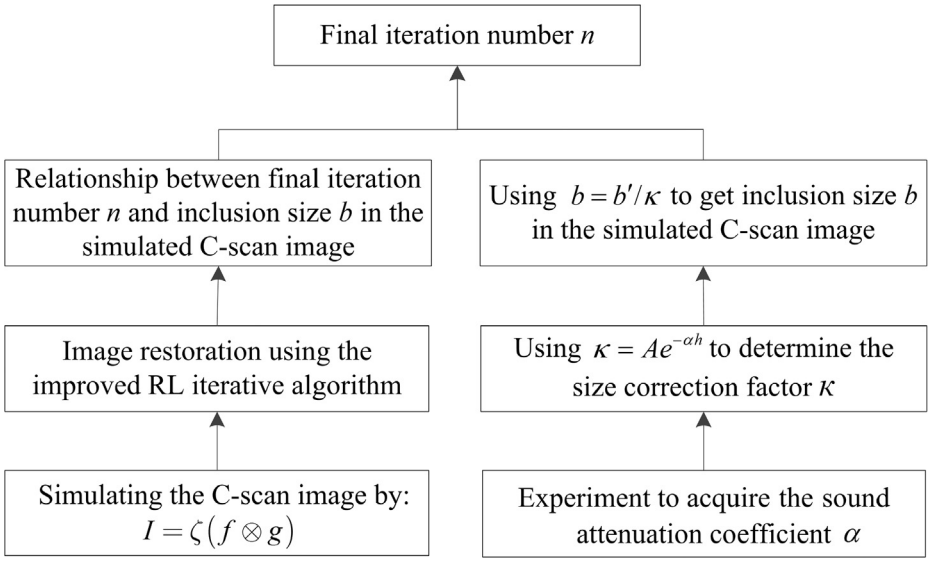

Fig. 7. Flowchart of the determination of final iteration number n.

$$n_{100}(b/\lambda_2) = \left\lceil \frac{1.466}{b/\lambda_2 - 1.737} \right\rceil \tag{12}$$

where $\lceil\ \rceil$ is the operator of round up to an integer. Eqs. (11) and (12) show that the dimensionless inclusion size b/λ_2 has a limiting size of 1.755 and 1.737 for the transducers of 50 MHz and 100 MHz. The limiting size represents the image size of an infinitely small object, i.e., the size of the PSF itself.

It should be noted that the simulated C-scan images do not consider any sound attenuation and experimental system effect. In practice, the strong attenuation and scattering of the sound waves are existed, and the electrical and electromechanical parts in ultrasonic system also influence the measured results. Therefore, a size correction factor κ is introduced and the relationship of inclusion sizes between simulated C-scan image and experimental C-scan image is expressed as

$$b = \frac{1}{\kappa} b' \tag{13}$$

where b' is the inclusion size measured in experimental C-scan image. $\kappa < 1$ indicates the inclusion size b' measured in experimental C-scan image is smaller than that of the simulated C-scan image. The size correction factor κ is a function of system impact factor A, sound

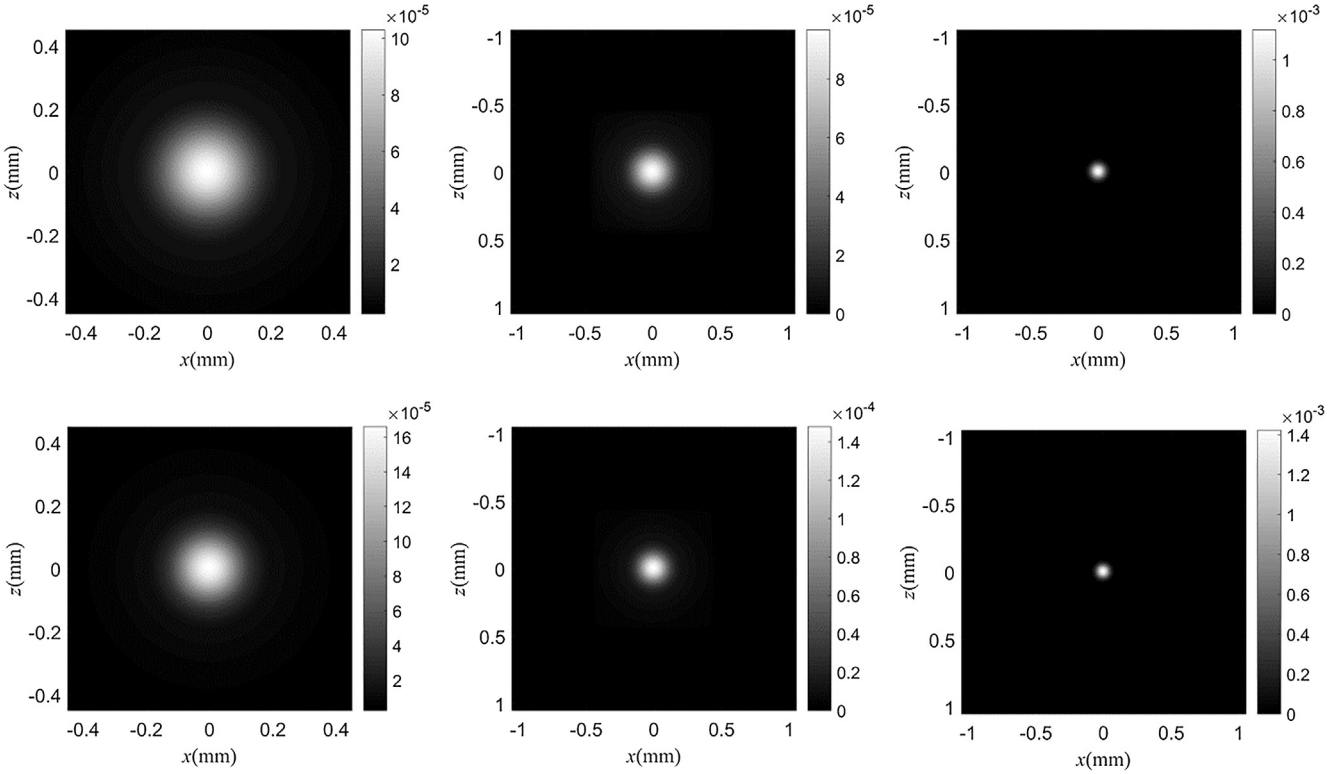

Fig. 8. The simulated results of an inclusion with true size of 50 μm. The left column are the PSFs of transducers with center frequency of 50 MHz and 100 MHz; the middle column are the simulated C-scan images using the corresponding PSFs; the right column are the restored C-scan images with final iteration number n = 64 and n = 16, respectively.

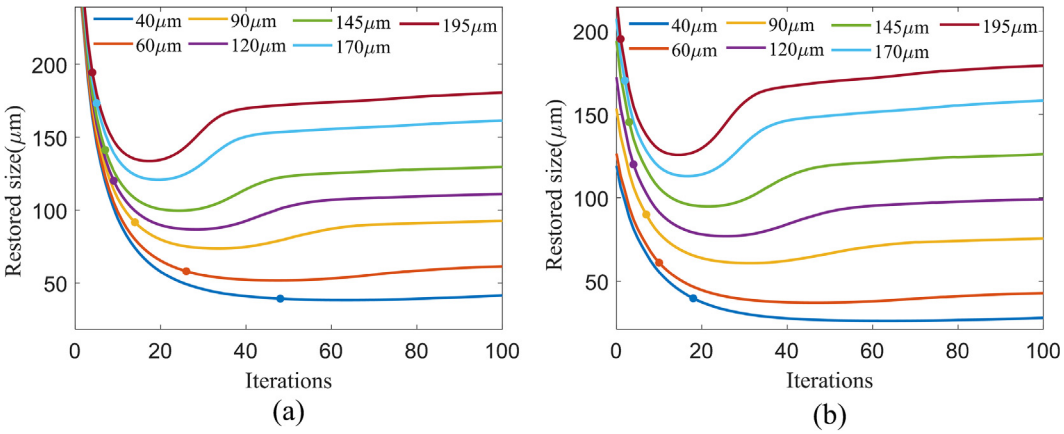

Fig. 9. The convergence of the inclusion size measured in restored C-scan images as a function of iteration numbers for different size of inclusions (a) 50 MHz (b) 100 MHz.

attenuation coefficient α and inclusion depth h, which is expressed as

$$\kappa = Ae^{-\alpha h} \tag{14}$$

The system impact factor A reflects the effect of all electrical and electromechanical parts on the results of ultrasonic imaging system. The attenuation coefficient α in Eq. (14) is determined by the equation [42]

$$\alpha = -\frac{1}{d}\ln\frac{P_2}{P_1} \tag{15}$$

where d is the thickness of specimen, P_1 and P_2 are the maximum absolute peaks of the first bottom echo wave and the second bottom echo wave. The attenuation coefficient α calculated by Eq. (15) is a comprehensive attenuation coefficient that contains the effects of different frequency components, which is determined using the maximum absolute peaks of the time-domain signals. Although the attenuation coefficient α and the size correction factor κ can be also calculated in the frequency-domain, they are proposed in this work to account for the effects of comprehensive attenuation and scattering of the waves encountered in practical experimental system on the finial iteration number n. Therefore, the attenuation coefficient α is not measured in the frequency-domain to illustrate the effects of frequency component on the attenuation coefficient α, as well as the size correction factor κ and finial iteration number n. It is a constant value for the experimental system with a certain transducer and testing material. Substituting Eq. (14) into Eq. (13), the relationship of inclusion sizes between simulated and experimental C-scan image can be expressed as

$$b = \frac{e^{\alpha h}}{A}b' \tag{16}$$

In Eq. (16), the system impact factor A is a constant for the same transducer, which can be measured from the calibration experiments. For a specific calibration experiment, the attenuation coefficient α, inclusion depth h and inclusion size b' are measured directly. Once the true size of the inclusion is measured by other means, such as Optical Microscope, the inclusion size b in the image can be obtained from the simulated C-scan image, and the system impact factor A is calculated. In addition, the system impact factor A is independent of the inclusion depth h. For the inclusion with greater depth, the transducer should be lowered to make it focus on the inclusion, so the true size of the inclusion can be also measured. Substituting Eq. (16) into Eqs. (11) and (12), the relationship between final iteration number n and dimensionless inclusion size b'/λ_2 in experimental C-scan image is expressed as

$$n_{50}(b'/\lambda_2) = \left\lceil \frac{0.824}{e^{\alpha h}b'/A\lambda_2 - 1.755} \right\rceil \tag{17}$$

$$n_{100}(b'/\lambda_2) = \left\lceil \frac{1.466}{e^{\alpha h}b'/A\lambda_2 - 1.737} \right\rceil \tag{18}$$

Eqs. (17) and (18) show that in order to determine the finial iteration number, it is need to measure the system impact factor A and attenuation coefficient α.

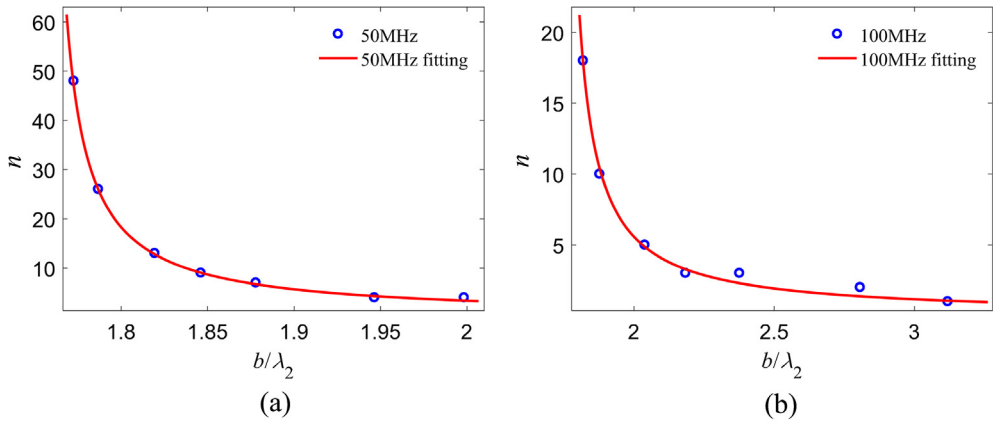

Fig. 10. The relationship between final iteration numbers n and dimensionless inclusion size b/λ_2 measured in simulated C-scan images for different transducers (a) 50 MHz (b) 100 MH.

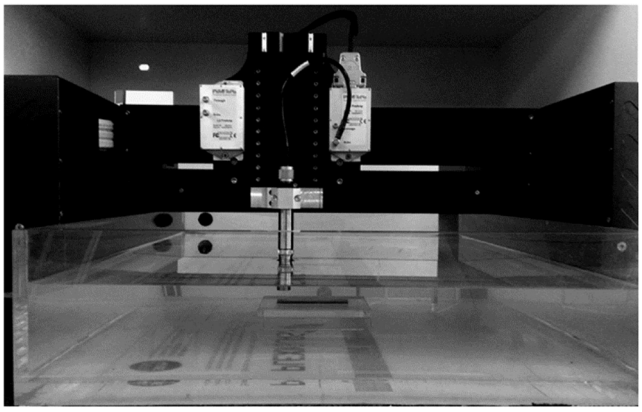

Fig. 11. Experimental setup of the immersion ultrasonic testing system.

3. Experimental measurement and verification

In order to determine the system impact factor A and prove the effectiveness of the improved RL iterative algorithm, the experiments of inclusions detection using immersion ultrasonic equipment PVA SAM300 are performed. The specimen is GCr15 bearing steel that is expected to contain Al_2O_3 inclusions internally. The acoustic impedance of the Al_2O_3 is 41.49MRayl, which is smaller than that of the steel matrix (45.39MRayl) [43]. The dimension of the specimen is 35 mm × 20 mm × 20 mm and its top surface is machined by a grinder. As is shown in Fig. 11, the specimen is immersed in a water tank and a spherically focused transducer is raster scanned from the top left to the bottom right of the specimen with a rough step of 20 μm, and then the local area that contains only one inclusion is imaged with a finer step of 2 μm. Two commercial spherically focused transducers PVA AS PT50 and PVA AS PT100 with nominal specifications of 50 MHz center frequency, 10 mm focal length and 100 MHz center frequency, 8 mm focal length are used to transmit and receive the longitudinal wave. The nominal apertures of both transducers are 3 mm. In the following sections, the system impact factor is calculated for the focused transducers of 50 MHz and 100 MHz, and four C-scan images that contain one inclusion for each are restored using the improved RL iterative algorithm and the accuracy of the inclusion size measured in restored C-scan images are also compared.

3.1. Calculation of system impact factor

Fig. 12 shows the C-scan image of the specimen using transducer PT100 and four inclusions can be detected within a depth of 1.0 mm. Based on this result, the local areas of 1 mm × 1 mm that contain inclusions 1# and 2#, respectively, are zoomed in using transducer PT50 and the local areas of 1 mm × 1 mm that contain inclusions 3# and 4# are zoomed in using transducer PT100.

In order to calculate the system impact factor A, the sound attenuation coefficient α of the two transducers are measured for the specimen. A sheet sample with dimension of 10 mm × 10 mm is cut from the specimen. The thickness of the sample is 0.92 mm, so that the second bottom echo wave can be received for both transducers. Fig. 13 shows the A-scan signals received by the transducer PT50 and PT100, respectively. Twenty A-scan signals of different positions are averaged to eliminate fluctuation of the 1st bottom echo wave (P1) and the 2nd bottom echo wave (P2). For the transducer PT50, $P_1 = 0.87$, $P_2 = 0.191$ and for the transducer PT100 $P_1 = 0.683$, $P_2 = 0.072$. The sound attenuation coefficients α for the two transducers are $\alpha = 0.824$ Np/mm and $\alpha = 1.223$ Np/mm, respectively.

The inclusion 1# and 3# are used to calculate the system impact factors A of transducer PT50 and PT100, respectively. Fig. 14 shows the A-scan signal of inclusion 1# and 3#, which includes the interface wave and defect echo wave. According to the time difference between interface wave and defect echo wave, the depths of inclusion 1# and 3# are $h = 0.823$ mm and $h = 0.745$ mm, with the longitudinal velocity in steel of 5988 m/s. Because the waveform of the interface wave has been over ranged, the zero-crossing point is used to represents the position of the wave packet and the time difference between the two wave packets is the time difference between the interface wave and the defect echo wave.

For the inclusion 1# and 3#, their sizes measured in experimental C-scan images are $b' = 109$ μm and $b' = 107$ μm, respectively. By cutting, grinding and polishing, the maximum cross sections of the inclusions are exposed to the Optical Microscope and their equivalent diameters are 50 μm and 71 μm, respectively. Accordingly, the system impact factors of the two transducers calculated using Eq. (16) are $A = 1.01$ and $A = 2.39$. The relevant parameters about the calculation of the system impact factors A are listed in Table 1.

3.2. Model verification and comparison with experiments

The improved RL iterative algorithm is applied to restore the C-scan images that contain inclusion 1# ~ 4#. According to the inclusion sizes

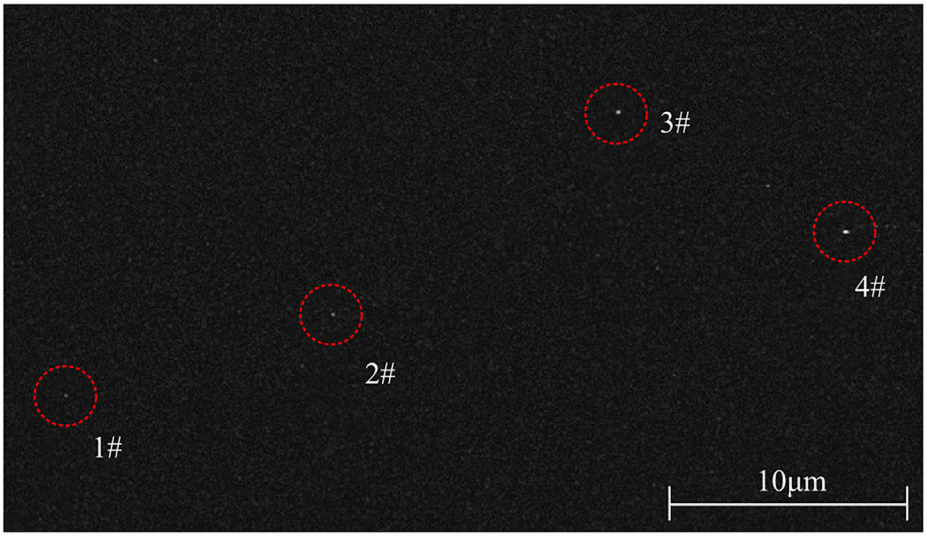

Fig. 12. C-scan image of the entire specimen with dimension of 35 mm × 20 mm × 20 mm.

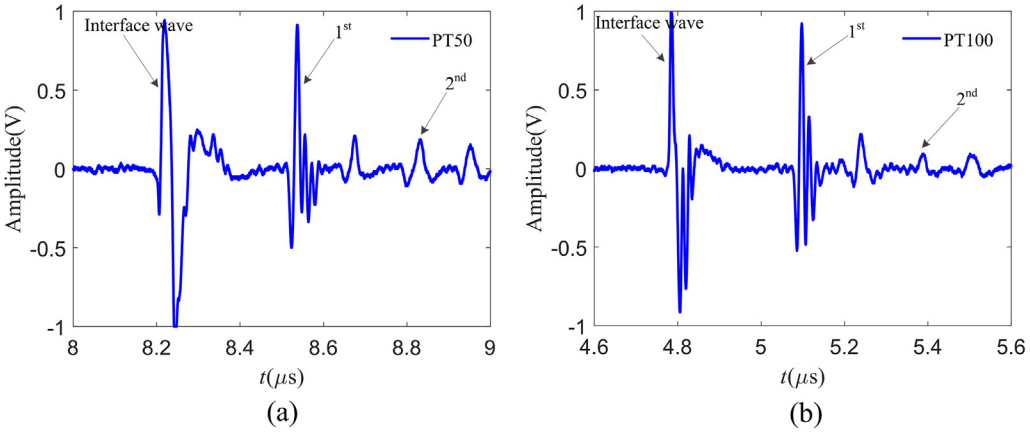

Fig. 13. The A-scan signals collected using different transducers (a) PT50 (b) PT100.

measured from the original C-scan images, the final iteration numbers n are determined using Eqs. (17) and (18). Fig. 15 shows the images of inclusion 1#∼4#. The first column is the optical micrographs of the four inclusions that show the maximum cross section, the second and third columns are the corresponding C-scan images before and after restoration. The aspect ratios of the four inclusions are almost the same, which can be approximated as spheres and the simulation of the C-scan image using circular inclusions is reasonable. The equivalent diameters of the four inclusions are calculated according to their area in optical micrographs. The second column indicates that the grains scattering is very strong, which produces noise in C-scan images. However, after restoration most noise has been reduced obviously, except for some with high level, as is shown in the third column. This result confirms that the final iteration number n determined by Eqs. (17) and (18) do not amplify the noise to the extent of affecting inclusion size measurement.

The inclusion sizes measured in second column and third column of the Fig. 15 are listed in Table 2. Table 2 shows that the inclusion sizes measured in restored images are much closer to their true sizes, which prove the effectiveness of the proposed method. However, it should be noted that the system impact factors A measured from inclusion 1# and 3# are also affected by the inclusion type. If the inclusions have different acoustic impedances or large aspect ratios, the error in measuring the size of inclusion will increase. For the specimen of GCr15 bearing steel, the type of inclusion 1#∼4# is mainly Al_2O_3, which guarantee the reliability of the measurement results.

4. Conclusions

In this work, an improved Richardson-Lucy iterative algorithm is proposed, which can be used to measure the inclusion size more accurately. The analytical expression of the PSF for the immersion ultrasonic imaging system is presented based on the MGB model and Kirchhoff approximation. The propagation properties of sound waves at water-steel interface and the spectral characteristics of the focused transducers with high frequency are considered, which helps to improve the accuracy of PSF. By restoring the simulated C-scan images using the improved RL iterative algorithm, the relationship between final iteration number and inclusion size in C-scan image is established. The size correction factor is introduced in the fitting function, which refers to the system impact factor, sound attenuation and inclusion depth and makes the fitting function applicable to different transducers and inclusions with different depth. Although the inclusion sizes measured in restored C-scan images are more accurate, determining the system impact factor by the calibration experiment still requires a lot of effort, which needs to measure the true size of a tested inclusion by other methods.

Acknowledgements

This work was supported by the National Natural Science Foundation of China [grant number 51775037]; Open Project Foundation of the State Key Laboratory of Traction Power in Southwest Jiaotong University [grant number TPL1713].

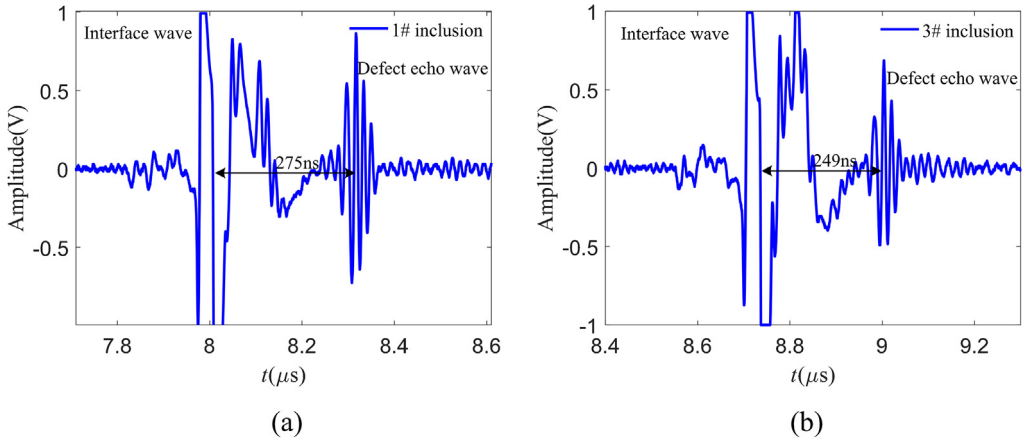

Fig. 14. A-scan signals of (a) inclusion 1# using transducer PT50 (b) inclusion 3# using transducer PT100.

Table 1
Relevant parameters for calculating the system impact factor *A*.

Inclusion no.	Frequency/MHz	Inclusion depth *h*/mm	attenuation coefficient α Np/mm	true size of inclusion/μm	Inclusion size b' in experimental C-scan image/μm
1#	50	0.823	0.824	50	109
3#	100	0.745	1.223	71	107

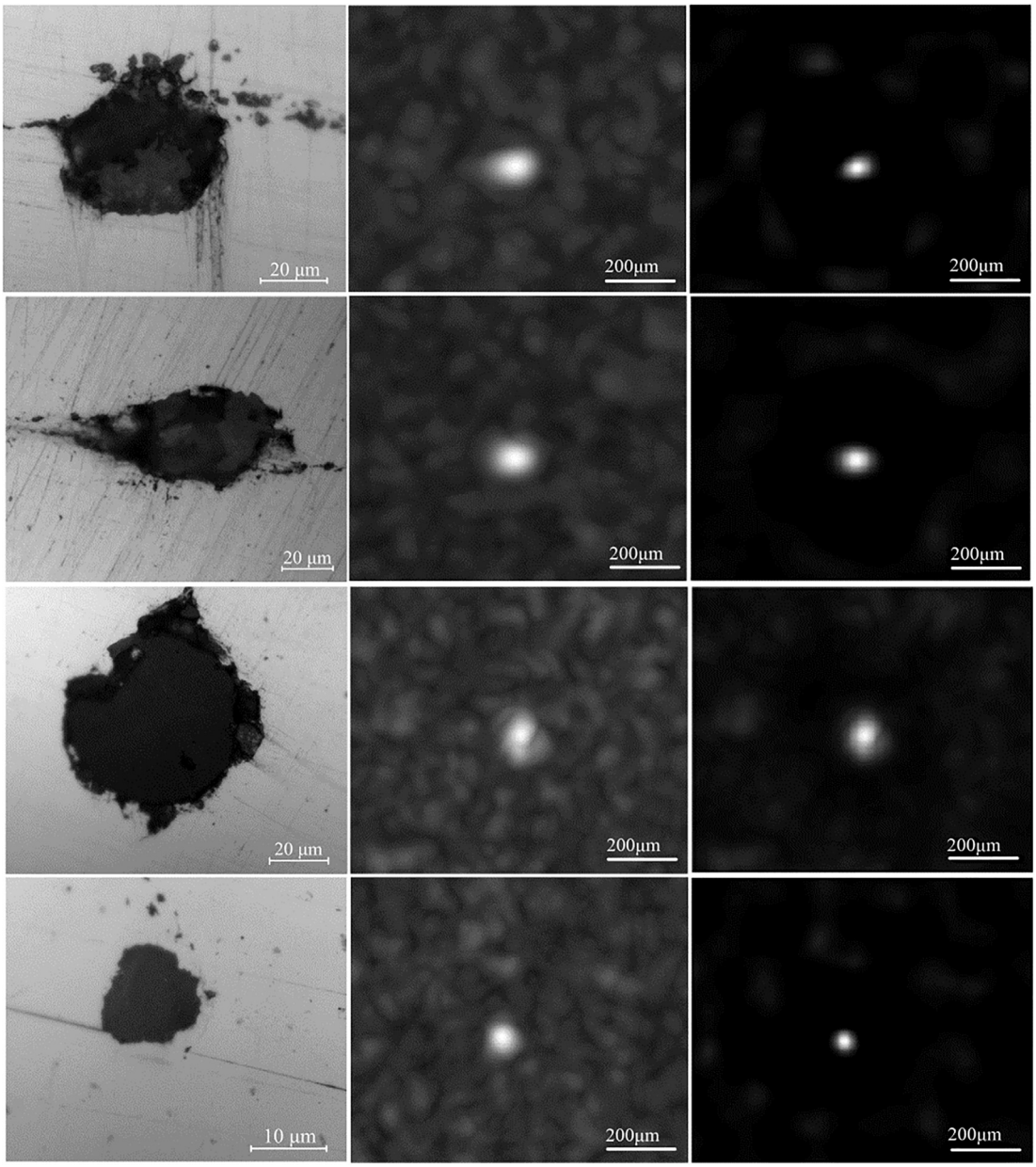

Fig. 15. Images of four different inclusions. The first column is optical micrographs. The second column is the original C-scan images. The third column is restored C-scan images. Each row represents one inclusion.

Table 2
Comparison of the results before and after restoration.

Number	Inclusion depth/mm	true size/μm	Blurred size/μm	Restored size/μm	Final Iteration number
1#	0.823	50	109	53	67
2#	0.862	60	106	64	37
3#	0.745	71	107	70	9
4#	0.913	41	84	39	30

References

[1] H. Atkinson, G. Shi, Characterization of inclusions in clean steels: a review including the statistics of extremes methods, Prog. Mater Sci. 48 (5) (2003) 457–520.
[2] P. Hu, J.A. Turner, C. Tarawneh, B. Wilson, A.J. Fuller, Multiple frequency ultrasonic detection of subsurface near-race inclusions for improved fatigue life performance, in: Proceeding of the 2015 Joint Rail Conference, American Society of Mechanical Engineers, 2015, pp. 1–5.
[3] Y. Ren, Y. Wang, S. Li, L. Zhang, X. Zuo, S.N. Lekakh, K. Peaslee, Detection of nonmetallic inclusions in steel continuous casting billets, Metall. Mater. Trans. B 45 (4) (2014) 1291–1303.
[4] H. Matsunaga, C. Sun, Y. Hong, Y. Murakami, Dominant factors for very-high-cycle

fatigue of high-strength steels and a new design method for components, Fatigue Fract. Eng. Mater. Struct. 38 (11) (2015) 1274–1284.
[5] D. Naragani, M.D. Sangid, P.A. Shade, J.C. Schuren, H. Sharma, J.-S. Park, P. Kenesei, J.V. Bernier, T.J. Turner, I. Parr, Investigation of fatigue crack initiation from a non-metallic inclusion via high energy x-ray diffraction microscopy, Acta Mater. 137 (2017) 71–84.
[6] B.G. Bartosiaki, J.A.M. Pereira, W.V. Bielefeldt, A.C.F. Vilela, Assessment of inclusion analysis via manual and automated SEM and total oxygen content of steel, J. Mater. Res. Technol. 4 (3) (2015) 235–240.
[7] Y.P. Bao, M. Wang, W. Jiang, A method for observing the three-dimensional morphologies of inclusions in steel, Int. J. Miner. Metall. Mater. 19 (2) (2012) 111–115.
[8] G.X. Zhang, Y.S. Hua, Y.W. Shen, H.W. Yang, The sensitivity of the focused ultrasonic method used in inclusion testing of the thick steel specimen, Appl. Mech. Mater. 455 (2014) 253–260.
[9] T.A. Bigelow, W.D. O'Brien, Scatterer size estimation in pulse-echo ultrasound using focused sources: theoretical approximations and simulation analysis, J. Acoust. Soc. Am. 116 (1) (2004) 578–593.
[10] T. Erlöv, T. Jansson, H.W. Persson, M. Cinthio, Scatterer size estimation using the center frequency assessed from ultrasound time domain data, J. Acoust. Soc. Am. 140 (4) (2016) 2352–2357.
[11] K. Raum, A. Ozguler, S.A. Morris, W.D. O'Brien, Channel defect detection in food packages using integrated backscatter ultrasound imaging, IEEE Trans. Ultrason. Ferroelectr. Freq. Control 45 (1) (1998) 30–40.
[12] Y. Song, Y. Wang, P. Ni, R. Qiao, X. Li, Flaw sizing method based on ultrasonic dynamic thresholds and neural network, in: 42nd Annual Review of Progress in Quantitative Nondestructive Evaluation: Incorporating the 6th European-American Workshop on Reliability of NDE, AIP Publishing, 1706 (1) (2016) pp. 1–9.
[13] M. Mihaljević, D. Markučič, B. Runje, Analysis of influential factors for ultrasonic disc size evaluation, Mater. Testing 57 (7–8) (2015) 674–679.
[14] O.V. Kolosov, G.A.D. Briggs, Acoustic Microscopy, Oxford University Press, New York, 2008.
[15] J. Núñez, A. Núñez, F.J. Montojo, M. Condominas, Improving space debris detection in GEO ring using image deconvolution, Adv. Space Res. 56 (2) (2015) 218–228.
[16] M. Prato, A. La Camera, S. Bonettini, M. Bertero, A convergent blind deconvolution method for post-adaptive-optics astronomical imaging, Inverse Prob. 29 (6) (2013) 1–22.
[17] C. Yu, C. Zhang, L. Xie, A blind deconvolution approach to ultrasound imaging, Ultrason., Ferroelectrics, Frequency Control, IEEE Trans. 59 (2) (2012) 271–280.
[18] Z. Chen, A. Basarab, D. Kouamé, Compressive deconvolution in medical ultrasound imaging, IEEE Trans. Med. Imaging 35 (3) (2016) 728–737.
[19] Y.W. Tai, P. Tan, M.S. Brown, Richardson-Lucy deblurring for scenes under a projective motion path, IEEE Trans. Pattern Anal. Mach. Intell. 33 (8) (2011) 1603–1618.
[20] W. Li, Q. Li, W. Gong, S. Tang, Total variation blind deconvolution employing split Bregman iteration, J. Vis. Commun. Image Represent. 23 (3) (2012) 409–417.
[21] E. Edrei, G. Scarcelli, Memory-effect based deconvolution microscopy for super-resolution imaging through scattering media, Sci. Rep. 6 (2016) 1–8.
[22] N. Meitav, E.N. Ribak, S. Shoham, Point spread function estimation from projected speckle illumination, Light Sci. Appl. 5 (2016) 1–7.
[23] D. Sage, L. Donati, F. Soulez, D. Fortun, G. Schmit, A. Seitz, R. Guiet, C. Vonesch, M. Unser, DeconvolutionLab2: An open-source software for deconvolution microscopy, Methods 115 (15) (2017) 28–41.
[24] X. Dai, Non-parametric efficiency estimation using Richardson-Lucy blind deconvolution, Eur. J. Oper. Res. 248 (2) (2016) 731–739.
[25] M. Laasmaa, M. Vendelin, P. Peterson, Application of regularized Richardson-Lucy algorithm for deconvolution of confocal microscopy images, J. Microsc. 243 (2) (2011) 124–140.
[26] C. Dalitz, R. Pohle-Frohlich, T. Michalk, Point spread functions and deconvolution of ultrasonic images, Ultrason., Ferroelectr., Frequency Control, IEEE Trans. 62 (3) (2015) 531–544.
[27] C.D. Claxton, R.C. Staunton, Measurement of the point-spread function of a noisy imaging system, JOSA A 25 (1) (2008) 159–170.
[28] M. Sapia, M. Fox, L. Loew, J.C. Schaff, Ultrasound image deconvolution using adaptive inverse filtering, Computer-Based Medical Systems, 1999, Proceedings 12th IEEE Symposium on, IEEE, 1999, pp. 248–253.
[29] R. Rangarajan, C. Krishnamurthy, K. Balasubramaniam, Ultrasonic imaging using a computed point spread function, Ultrason., Ferroelectr., Frequency Control, IEEE Trans. 55 (2) (2008) 451–464.
[30] H.J. Kim, S.J. Song, L.W. Schmerr, An ultrasonic measurement model using a multi-Gaussian beam model for a rectangular transducer, Ultrasonics 44 (8) (2006) 969–974.
[31] C.J. Bouwkamp, Diffraction theory, Rep. Prog. Phys. 17 (1) (1954) 35–100.
[32] N. Dey, L. Blanc-Feraud, C. Zimmer, P. Roux, Z. Kam, J.C. Olivo-Marin, J. Zerubia, Richardson-Lucy algorithm with total variation regularization for 3D confocal microscope deconvolution, Microsc. Res. Tech. 69 (4) (2006) 260–266.
[33] W.H. Richardson, Bayesian-based iterative method of image restoration*, JOSA 62 (1) (1972) 55–59.
[34] L.B. Lucy, An iterative technique for the rectification of observed distributions, Astronom. J. 79 (6) (1974) 745.
[35] H. Xiao, Y. Sun, D. Chen, J. Xu, Prediction of flat-bottom hole signals received by a spherically focused transducer for an ultrasonic pulse echo immersion testing, Meas. Sci. Technol. 27 (11) (2016) 1–11.
[36] J. Wen, M. Breazeale, A diffraction beam field expressed as the superposition of Gaussian beams, J. Acoust. Soc. Am. 83 (5) (1988) 1752–1756.
[37] P. Goldsmith, Quasioptical Systems: Gaussian Beam Quasioptical Propogation and Applications, vol. 5, IEEE Press, 1998, pp. 359–405.
[38] S. Chatillon, C. Poidevin, N. Gengembre, A. Lhémery, Simplified modeling of backscattered noise and attenuation phenomena for quantitative performance demonstration of UT methods, in: AIP Conference Proceedings, IOP Institute of Physics Publishing ltd, (2003), pp. 93–100.
[39] J.L. Rose, Ultrasonic Waves in Solid Media, Cambridge University Press, 2004.
[40] P. Karpur, B.G. Frock, Two dimensional pseudo-Wiener filtering in ultrasonic imaging for nondestructive evaluation applications, in: Review of Progress in Quantitative Nondestructive Evaluation, Springer, 1989, 743-750.
[41] M.A. Sapia, L.M. Loew, M.D. Fox, J.C. Schaff, Ultrasound image deconvolution using adaptive inverse filtering, in: IEEE Symposium on Computer-based Medical Systems, 1999, pp. 248–253.
[42] M. Aghaie-Khafri, F. Honarvar, S. Zanganeh, Characterization of grain size and yield strength in AISI 301 stainless steel using ultrasonic attenuation measurements, J. Nondestr. Eval. 31 (3) (2012) 191–196.
[43] D. Chen, H.F. Xiao, M. Li, J.W. Xu, A study on the inclusion sizing using immersion ultrasonic C-scan imaging, in: 12th International Conference on Damage Assessment of Structures, 842(1) (2017) pp. 1–8.